

Experimental Demonstration of a Magnetically Induced Warping Transition in a Topological Insulator Mediated by Rare-Earth Surface Dopants

Beatriz Muñiz Cano, Yago Ferreiros, Pierre A. Pantaleón, Ji Dai, Massimo Tallarida, Adriana I. Figueroa, Vera Marinova, Kevin García-Díez, Aitor Mugarza, Sergio O. Valenzuela, Rodolfo Miranda, Julio Camarero, Francisco Guinea, Jose Angel Silva-Guillén, and Miguel A. Valbuena*



Cite This: *Nano Lett.* 2023, 23, 6249–6258



Read Online

ACCESS |



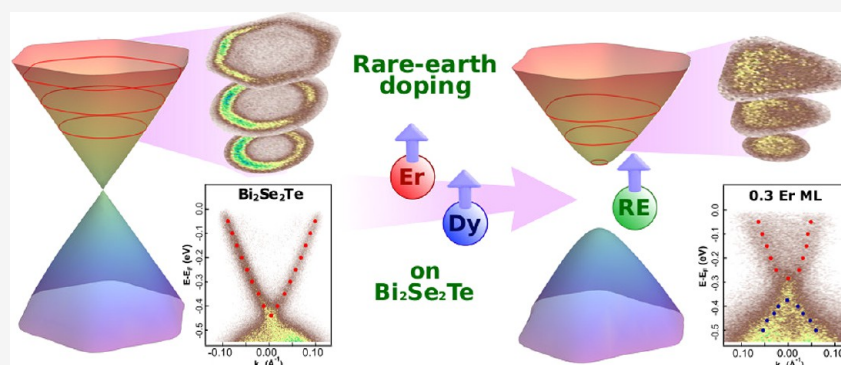
Metrics & More



Article Recommendations



Supporting Information



ABSTRACT: Magnetic topological insulators constitute a novel class of materials whose topological surface states (TSSs) coexist with long-range ferromagnetic order, eventually breaking time-reversal symmetry. The subsequent bandgap opening is predicted to co-occur with a distortion of the TSS warped shape from hexagonal to trigonal. We demonstrate such a transition by means of angle-resolved photoemission spectroscopy on the magnetically rare-earth (Er and Dy) surface-doped topological insulator $\text{Bi}_2\text{Se}_2\text{Te}$. Signatures of the gap opening are also observed. Moreover, increasing the dopant coverage results in a tunable p-type doping of the TSS, thereby allowing for a gradual tuning of the Fermi level toward the magnetically induced bandgap. A theoretical model where a magnetic Zeeman out-of-plane term is introduced in the Hamiltonian governing the TSS rationalizes these experimental results. Our findings offer new strategies to control magnetic interactions with TSSs and open up viable routes for the realization of the quantum anomalous Hall effect.

KEYWORDS: magnetic topological insulators, rare-earth doping, topological surface state, time-reversal symmetry breaking, angle-resolved photoemission spectroscopy, quantum anomalous Hall effect

Topological insulators (TIs) define a state of matter where the strong spin–orbit interaction (SOI) induces an exotic metallic topological surface state (TSS) with relativistic, Dirac-like, band dispersion with the spin locked to the momentum in an otherwise insulating material.^{1,2} Magnetic impurities interaction with the TSSs is especially attractive in these materials due to the emergence of novel quantum phenomena with relevant fundamental and technological implications in spintronics and quantum information processing.³ The combination of topological properties and magnetic order can lead to new quantum states of matter as the quantum anomalous Hall effect (QAHE), characterized by purely spin-polarized dissipationless currents without an external magnetic field.^{4,5}

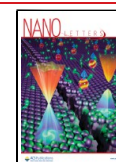
When magnetism is introduced by impurity doping with magnetic elements, either via substitutional or surface

doping,^{6–9} magnetic extension,¹⁰ or proximity coupling to magnetic layers,^{11,12} the TI becomes magnetic (MTI), and the time-reversal symmetry (TRS) can be broken, magnetically inducing the opening of a bandgap at the Dirac point (DP) of the TSS.^{6,7} If this gap is tuned to the Fermi level (E_F), the QAHE can be realized as it was first experimentally observed in Cr- and V-doped $(\text{Bi,Sb})_2\text{Te}_3$ thin films.^{13,14} Recent discoveries based on the magnetic extension of TIs, as the first

Received: February 15, 2023

Revised: April 24, 2023

Published: May 8, 2023



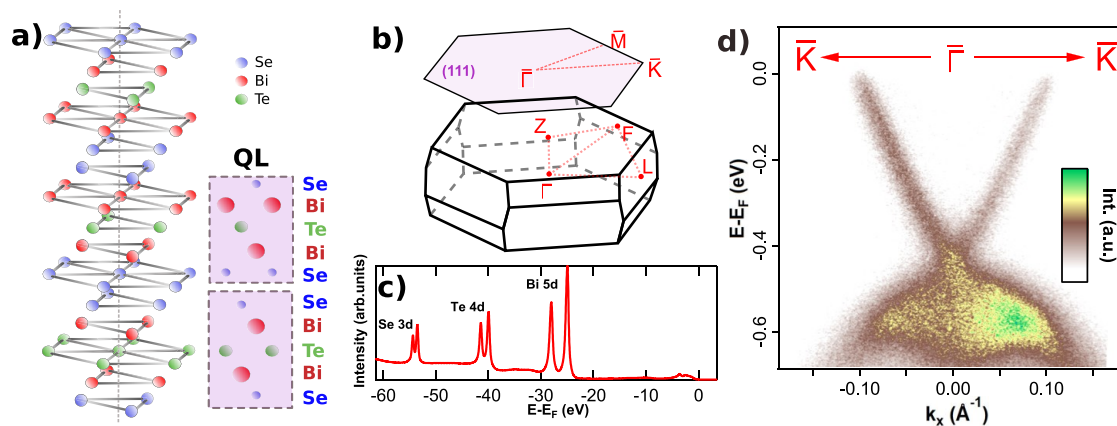


Figure 1. Pristine $\text{Bi}_2\text{Se}_2\text{Te}$ crystal structure and characterization. (a) 3D quintuple layer crystal structure and (b) Brillouin zone (BZ) and projected surface BZ of $\text{Bi}_2\text{Se}_2\text{Te}$. (c) XPS spectrum (Se 3d, Te 4d, Bi 5d, and valence band) of the pristine $\text{Bi}_2\text{Se}_2\text{Te}$ single crystal measured at a photon energy of $h\nu = 100$ eV and at $T = 15$ K. (d) ARPES bandmap of the pristine $\text{Bi}_2\text{Se}_2\text{Te}$ TSS along the $\overline{\Gamma\text{K}}$ direction acquired at $h\nu = 52$ eV and at $T = 15$ K.

antiferromagnetic (AFM) TI, MnBi_2Te_4 ^{15,16} have opened up new perspectives for the realization of these quantized topological effects in intrinsically magnetic stoichiometric compounds. However, these systems heavily depend on sophisticated and complex growth methods, resulting in variations in the density of structural defects, eventually leading to drastic changes in the electronic structure of the TSSs (opening or not of an intrinsic magnetic gap at the DP) or affecting its magnetic properties (formation or not of antiferromagnetic order).¹⁷ Similar discrepancies have been found because of inhomogeneities of the spatial distribution of bulk magnetic dopants.^{18,19}

Surface doping offers an alternative to separate the two aforementioned critical processes, namely, growth and doping, limiting the dopant's presence to where the TSSs are most sensitive to their effects and maximizing the magnetic anisotropy by the lower coordination symmetry.²⁰ Experimental attempts at magnetically doped TI surfaces also indicate that achieving control on the magnetic ground state and anisotropy is challenging due to the existence of multiple adsorption sites, strong surface relaxations, and significant doping of the bulk states from defects or inhomogeneities.^{21–24} Although gaplike features have been interpreted as magnetically induced, numerous factors such as momentum and energy spatial fluctuations near the DP²⁵ or surface chemical modifications^{26–28} may contribute to the observation of a gap. Furthermore, the DP can be buried into the bulk band projections, making the possible gap opening undetectable by techniques such as angle-resolved photoemission spectroscopy (ARPES). These ambiguities show the necessity to go beyond the present state-of-the-art in the development of these doping strategies.

An alternative route to this problem is to surface dope TIs with magnetic rare-earths (REs) whose larger size can prevent the occurrence of substitutional sites at the surface, reducing the multiplicity of adsorption configurations²⁹ and enhancing the magnetic anisotropy. Likewise, RE large magnetic moments, originating from the unpaired 4f electrons,³⁰ can maximize the magnetically induced gap hosting the spin-polarized currents⁷ and also allow a lower doping concentration,³¹ which could eventually lead to a robust QAHE at higher temperatures.³ In particular, Er clusters have been shown to exhibit hysteresis and out-of-plane magnetic

anisotropy by X-ray magnetic circular dichroism (XMCD) at very low temperatures on close metal-packed surfaces.³² Similarly, Er or Dy single atoms can exhibit out-of-plane magnetic anisotropy.³³ Even more, Dy single atoms may experience magnetization relaxation time scales as large as 1000 s on several nonmetallic substrates.^{34,35} Besides, REs deposited on metals can be efficiently coupled via itinerant s and p electrons of the metal to achieve ferromagnetism with Curie temperatures as high as 80 K.^{36,37} RE bulk substitutional doping with Eu,^{38,39} Gd,⁴⁰ Dy,³¹ or Ho^{41,42} on Bi_2Te_3 thin films has been achieved. Even though the TSSs are preserved despite RE large magnetic moments, all films remained essentially paramagnetic or weak AFM. Regarding the bandgap opening, massive Dirac fermions have only been observed for a given concentration of Dy-doped Bi_2Te_3 thin films,⁴¹ attributed to inhomogeneous and short-range ferromagnetic patches.^{3,43} Magnetic proximity effects have also been explored on EuS layers on TI thin films with neither significant induced magnetism nor an enhancement of the Eu magnetic moment at the interface.⁴⁴

Recently, the magnetic order in MTIs, particularly in the newly discovered MnBi_2Te_4 family,⁴⁵ has been theoretically predicted not only to open a gap at the DP but also to lower the Dirac cone's warping symmetry from hexagonal to trigonal, alongside an induction of a gap opening at the DP.^{46–49} Notably, this trigonal warping at the magnetically ordered phase is sensitive to the direction of a net surface magnetic moment, providing an effective approach for the detection of magnetic ordering effects on the TSSs when the gap cannot be unequivocally resolved and/or related to the TRS breaking by out-of-plane magnetic moments. However, an experimental observation of these phenomena is still lacking.

Herein, by means of ARPES, we report the effects on the TSS of the prototypical three-dimensional (3D) TI, $\text{Bi}_2\text{Se}_2\text{Te}$, doped with RE impurities (Er and Dy). As expected, the pristine surface features hexagonal warped TSSs which, as the RE atoms are deposited even for small coverages, exhibit the predicted transition from hexagonal to trigonal, providing the first experimental evidence of such magnetically induced warping modification. In addition, with the systematic doping, signatures of a bandgap opening at the DP are found, whereas the chemical potential is gradually modified, resulting in a controllable p-type doping. This allows us to tune the DP

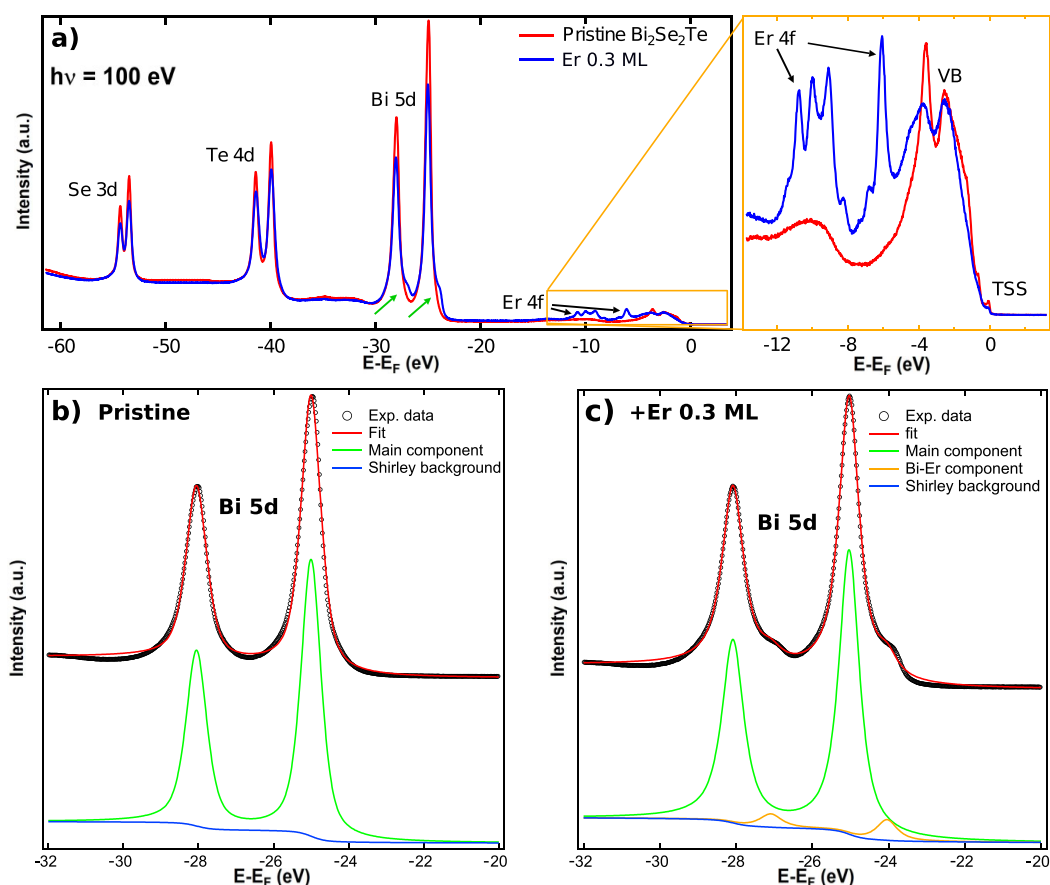


Figure 2. XPS characterization of Er-doped $\text{Bi}_2\text{Se}_2\text{Te}$ acquired with a photon energy of $h\nu = 100$ eV and at $T = 15$ K. (a) Comparison of the XPS spectra of pristine (red line) and 0.3 monolayer (ML) Er/ $\text{Bi}_2\text{Se}_2\text{Te}$ (blue line). A second component of the Bi 5d peak is developed after Er deposition (green arrows). Right: zoom-in on the Er 4f states and the $\text{Bi}_2\text{Se}_2\text{Te}$ valence band energy range. Multipeak fit of XPS data for (b) the pristine sample and (c) the 0.3 ML Er-doped sample. A second component (orange) is related to the Er–Bi interaction, as its area is proportional to the Er coverage (see SM, Figures S1 and S3).

energy closer to the E_F , thus fulfilling the prerequisites for the realization of the QAHE. When the Hamiltonian governing the TSS considers a net magnetic moment, with an exchange field coupling of ≈ 0.1 eV, the experimental observations are rationalized.

Ternary $\text{Bi}_2\text{Se}_2\text{Te}$ single crystals⁵⁰ were grown by a modified Bridgman method in a standard crystal growth system and characterized by X-ray powder diffraction and Raman spectroscopy (see Supporting Information (SM), section I), showing high crystal quality and crystalline long-range order. The crystals were exfoliated *in situ* at $T = 15$ K (base temperature), and the surface quality and crystal structure were further verified by low energy electron diffraction (LEED) at base temperature before and after RE deposition. The obtained LEED patterns do not show any evidence of surface reconstructions originating from the RE dopants (see SM, Figure S14 in section VIII). X-ray photoemission spectroscopy (XPS) and ARPES measurements were performed on the *in situ* exfoliated single crystals with a MBS hemispherical analyzer at the LOREA beamline^{51,52} in ALBA Synchrotron, with linear horizontal polarization and photon energies of $h\nu = 100$ and 52 eV, respectively. Er and Dy were sublimated with an e-beam evaporator. The deposition rates and coverages were calibrated with a quartz crystal microbalance and correlated with the attenuation of the XPS Bi 5d core level (see Figure S1 in SM, section II). XPS and ARPES measurements were also performed at $T = 15$ K, well below

the expected Curie temperature of Er and Dy clusters,⁵³ so a magnetic ordering of the RE surface dopants can be expected.

The $\text{Bi}_2\text{Se}_2\text{Te}$ quintuple layer (QL) three-dimensional (3D) crystal structure and the Brillouin zone (BZ) and its projected surface Brillouin zone (SBZ) are sketched in Figure 1(a),(b), respectively. As previously commented, $\text{Bi}_2\text{Se}_2\text{Te}$ bulk single crystals were mechanically exfoliated *in situ* at 15 K to minimize the induced density of defects. The high sample quality is derived, apart from the aforementioned LEED patterns in SM, from the XPS spectrum (Figure 1(c)), showing highly intense and narrow peaks with no signs of oxidation, contamination, or large disorder²⁸ for the Se 3d, Te 4d, and Bi 5d core levels. The very well-defined spin–orbit doublets as compared to isostructural TI films grown by molecular beam epitaxy prove the surface quality after *in situ* exfoliation.^{54–56}

The pristine $\text{Bi}_2\text{Se}_2\text{Te}$ TSS ARPES bandmap along the ΓK direction is shown in Figure 1(d). The DP is located 440 meV below the E_F , outside the bulk projection bandgap, and the Fermi velocity is $v_F \sim (7.1 \pm 0.2) \times 10^5$ m/s, estimated from $1/\hbar(\partial E/\partial k)$,⁵⁷ consistent with previous works.^{57,58}

Figure 2(a) displays XPS spectra, showing the main effects on the core levels and the valence band (VB) states induced by Er deposition, as compared to the pristine sample. The Se 3d, Te 4d, and Bi 5d core levels are attenuated (SM, Figure S3 in section III). No extra components are detected at higher binding energies (left side of the peaks), consistent with the

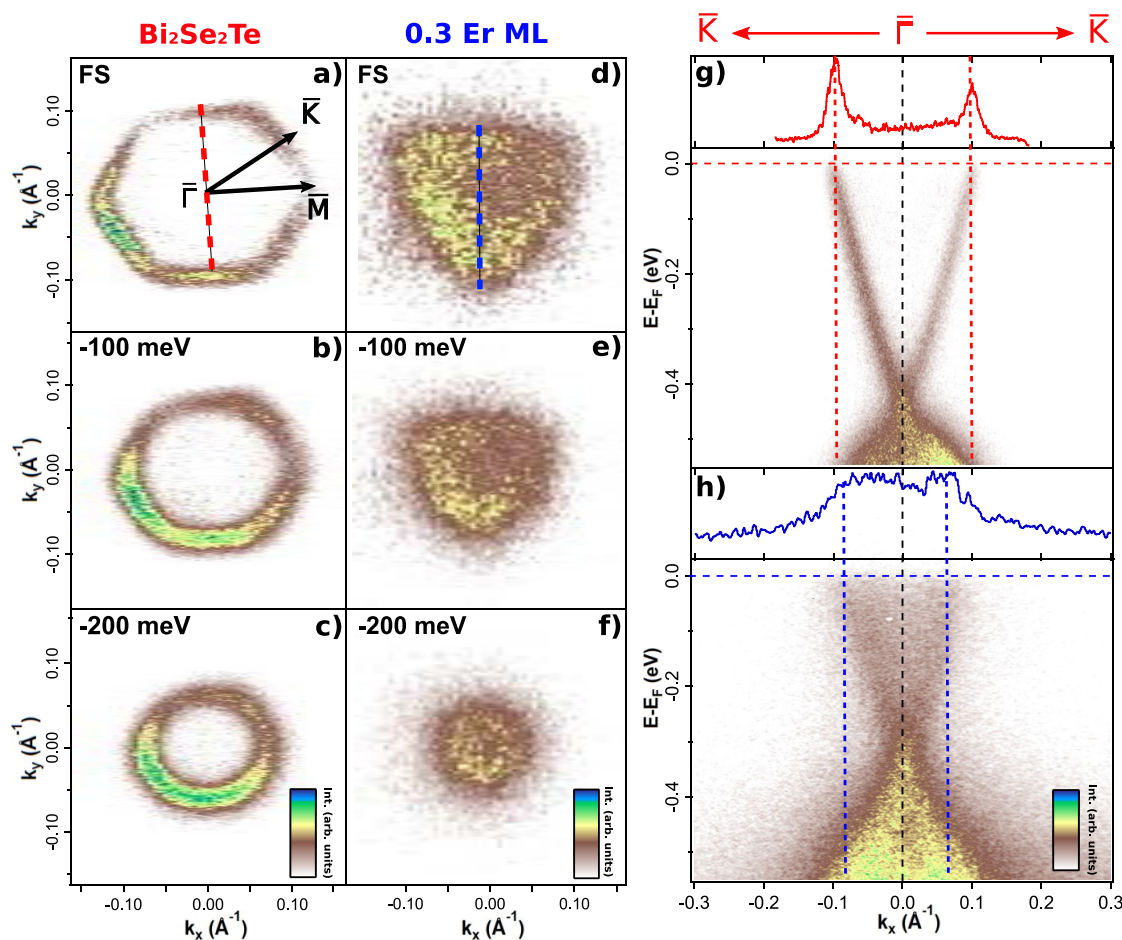


Figure 3. Experimental observation by ARPES of the magnetically induced hexagonal to trigonal TSS warping transition upon Er deposition. (a)–(c) Fermi surfaces and constant energy maps at 100 and 200 meV below the Fermi level (E_F) for pristine $\text{Bi}_2\text{Se}_2\text{Te}$, showing the hexagonal warping of the topological surface state (TSS). (d)–(f) Same as in (a)–(c) for 0.3 monolayer (ML) $\text{Er}/\text{Bi}_2\text{Se}_2\text{Te}$, showing the induced trigonal warping of the TSS. TSS bandmaps along the $\overline{\Gamma}\text{K}$ direction (red and blue dashed lines in (a) and (d)) for (g) pristine and (h) 0.3 ML $\text{Er}/\text{Bi}_2\text{Se}_2\text{Te}$, acquired with a photon energy $h\nu = 52$ eV and at $T = 15$ K. Momentum distribution curves (MDCs) extracted at the E_F are shown on the top of each bandmap. The induction of a trigonal warping in the TSS is also evidenced by the Fermi wavevector k_F and Fermi velocity v_F asymmetry around the $\overline{\Gamma}$ point for the Er-doped system in (h).

absence of surface oxidation or contamination. Additionally, no further disorder is introduced since no widening of the peak line shapes is detected, also evidenced by the very sharp, well resolved multipoint structure of highly localized and, in principle, weakly interacting (nondispersive) Er 4f states at $E - E_F = 5\text{--}12$ eV (magnified in the inset in Figure 2(a)). The multipoint fit of the XPS spectra in Figures 2(b),(c) was used for the estimation of the Er coverage. ARPES VB maps acquired at this energy region are included in the SM, Figure S2 in section III.

Remarkably, a second Bi 5d component is developed at lower binding energies (green arrows in Figure 2(a) and orange curve in Figure 2(c)). These feature intensity that linearly increases with the Er coverage (SM, Figures S1 and S3), demonstrating its relationship with a superficial Bi–Er bond and revealing a degree of interaction at the RE–TI interface. Based on a simple electronegativity analysis, we attribute the change in the line shape of Bi 5d to the charge transfer produced by the deposition of Er. The partial charge given by Er is then shared with the more oxidized species (Bi^{3+}), although the substrate is Se-terminated. However, intrinsic native point defects naturally occur in binary or ternary tetradymite TIs as vacancies, antisites, or interstitial

atoms at the van der Waals gap between QLs.⁵⁹ As a result, a significant macroscopic concentration of Bi atoms about 1–5% ML^{17,59} cannot be excluded at the outermost surface. Besides, it has also been shown that when REs (i.e., Dy) are introduced as substitutional dopants on Bi_2Te_3 thin films they tend to occupy Bi substitutional sites on Bi layers,⁶⁰ highlighting that RE dopants are prone to ionic or covalent bonding with Bi. This effect is also reflected in an energy shift as the Er content increases (see SM, Figure S1 in section II). A similar behavior has been observed for other metal–TI interfaces in the same Bi 5d state.⁵⁵ The same Bi 5d second component also appears in Dy-doped $\text{Bi}_2\text{Se}_2\text{Te}$ (SM, Figure S5 in section IV).

The Fermi surface (FS) and constant energy (CE) maps for pristine and 0.3 monolayer (ML) $\text{Er}/\text{Bi}_2\text{Se}_2\text{Te}$ are shown in Figure 3. Pristine $\text{Bi}_2\text{Se}_2\text{Te}$ TSS exhibits the hexagonal warped FS and the circular-like shaped lower energy CE maps expected for rhombohedral 3D TIs (Figures 3(a)–(c)). The warping strength is consistent with the literature, being similar to most warped TSSs, as in Bi_2Te_3 ,^{61,62} and higher than in isostructural $\text{Bi}_2\text{Te}_2\text{Se}$ ⁶³ or Bi_2Se_3 ,⁶⁴ whose warping effects are smoother or even negligible. When depositing Er, the FS and CE maps drastically change. Upon the 0.3 Er ML, the TSS warping symmetry evolves from hexagonal to trigonal (Figures

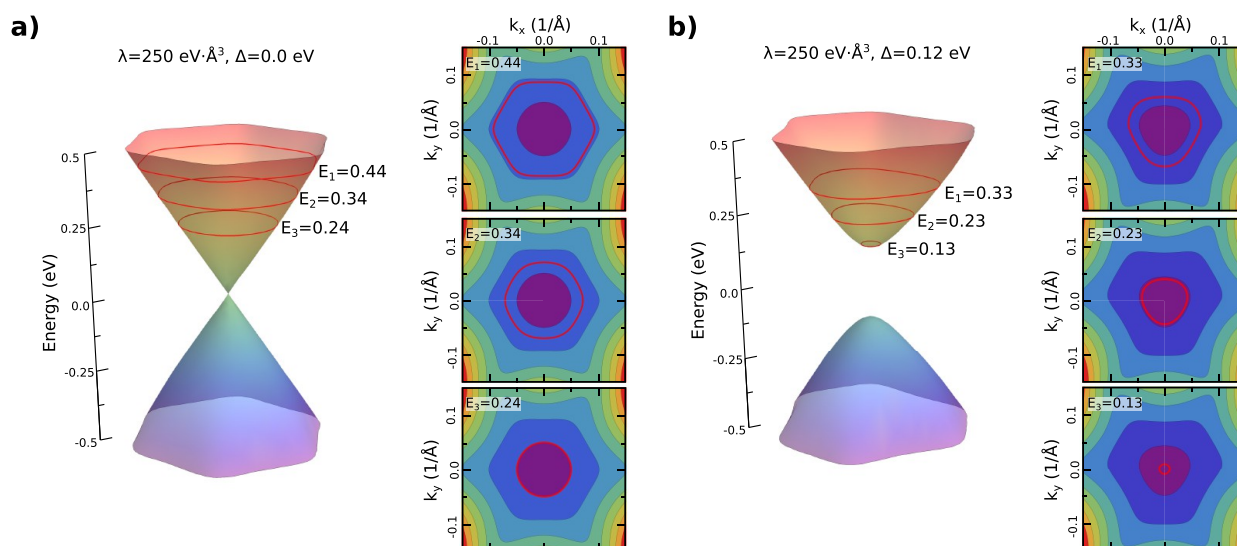


Figure 4. Theoretical modeling of the TSS band structure and the warping transition. Band structure of the surface state of a topological insulator and the evolution of the constant energy (CE) maps (red lines) as a function of the Fermi energy for the (a) pristine system, with $v_F = 7.1 \times 10^5$ m/s and $\lambda = 250$ eV·Å³, and (b) the system with magnetic impurities, with $\Delta = 0.12$ eV. The transition from a hexagonal to a trigonal warping, as well as the induction of a gap, is observed. The small panels display CE maps at three different energies relative to the Dirac point, corresponding to the energies of the experimental ones.

3(d)–(f)), clearly away from the DP and closer to E_F . Similar modifications in the Dirac cone warping, from hexagonal to trigonal, have been predicted below the magnetic ordering temperature in the family of $\text{MnBi}_{2m}\text{Te}_{3m+1}$ MTIs.⁴⁷

To give some insight into the warping transition of the TSS, the description of an undoped TI using the model developed by Fu⁶¹ can be applied, in which the low energy dispersion of the system is described by the following Hamiltonian

$$H = \hbar v_F(k_x \sigma_y - k_y \sigma_x) + \frac{\lambda}{2}(k_+^3 + k_-^3) \sigma_z \quad (1)$$

with $k_{\pm} = k_x \pm ik_y$. The last term is only invariant under 3-fold rotation and responsible for the hexagonal warping.^{46,47,61} The 3D band dispersion of the system is shown in Figure 4(a), where the previously calculated $v_F = 7.1 \times 10^5$ m/s was used to match the experiment. The warping parameter λ was set to 250 eV·Å³ by fitting the theoretical CE map at 0.440 eV (right-hand side of Figure 4(a)) to the measured one (Figure 3(a)). This value confirms a similar warping strength compared to other TIs such as Bi_2Te_3 .⁶¹ The energy values (with respect to the DP) in the theoretical CE maps (Figure 4(a)) were chosen to match the experiment (Figures 3(a)–(c)). As expected, the hexagonal warping can be clearly distinguished far from the DP, whereas when approaching the DP, the CE maps round off, as in the experiment (Figure 3(a)–(c)).

To introduce the effect of the RE dopants in the former Hamiltonian (eq 1), a magnetic moment can be coupled to the TI TSS via an exchange interaction⁴⁷ through a Zeeman-like term. The Hamiltonian takes the final form (see SM, section V)

$$H = \hbar v_F(k_x \sigma_y - k_y \sigma_x) + (\lambda k^3 \cos 3\theta - \Delta) \sigma_z \quad (2)$$

where Δ stands for the exchange coupling and θ for the azimuthal angle of the momentum. Δ is a fitting parameter of our model. At this point the model keeps using the previously obtained values of v_F and λ , that is 7.1×10^5 m/s and 250 eV·Å³, in such a way that the only difference between the pristine and Er-doped models is the inclusion of the Zeeman-like term

carrying the fitting parameter Δ . The Δ value is then changed until the theoretical CE maps match the experimental ones (Figures 3(d)–(f)), finally obtaining an optimized correspondence with $\Delta = 0.12$ eV (see SM, Figure S7 in section V, for more details). The theoretical results are shown in Figure 4. Note that the E_F (with respect to the DP) is modified by the introduction of the RE dopants (Figures 3(g),(h)), so the values of the energies for the theoretical CE maps have been accordingly changed. Also and as a direct consequence of the warping transition, asymmetric k_F values are found as a consequence of the different theoretically obtained v_F of 9.8×10^5 m/s and 8.2×10^5 m/s, respectively, for the flat and corner sides of the trigonal TSS (see SM, Figure S8 in section VI, for more details).

The energy dispersion of the system with the above set of parameters is shown on the left-hand side of Figure 4(b), with the TSS band presenting a gap of 240 meV as a consequence of the nonvanishing net magnetization induced by the magnetic dopants. Furthermore, the TRS is broken, and the surface of the TI becomes a quantum anomalous Hall (or Chern) insulator.^{1,65} As seen on the CE maps (right-hand side of Figure 4(b)), the TRS breakdown results in the transition from the 6-fold to a 3-fold rotational symmetry (see section V in SM), so that the warped FS evolves from hexagonal (pristine) to trigonal (doped system), as in the experiments (Figures 3(d)–(f)). Interestingly, the obtained value of Δ is up to 1 order of magnitude larger than previous expectations.^{66–69} Although higher values have been predicted or expected,^{70,71} up to our knowledge, this is the first time that the exchange coupling has been estimated by direct comparison to experimental results. Such a relatively high value of the exchange coupling Δ makes Bi_2Se_3 doped with RE a good candidate system for the realization of the QAHE.

Experimentally, the change in the warping symmetry is also evidenced, just as in the theoretical model, by the induced inversion asymmetry in the TSS band dispersion in Figure 3(g),(h), measured along the $\overline{\Gamma K}$ direction (red and blue dashed lines in Figures 3(a) and (d)), and in the momentum

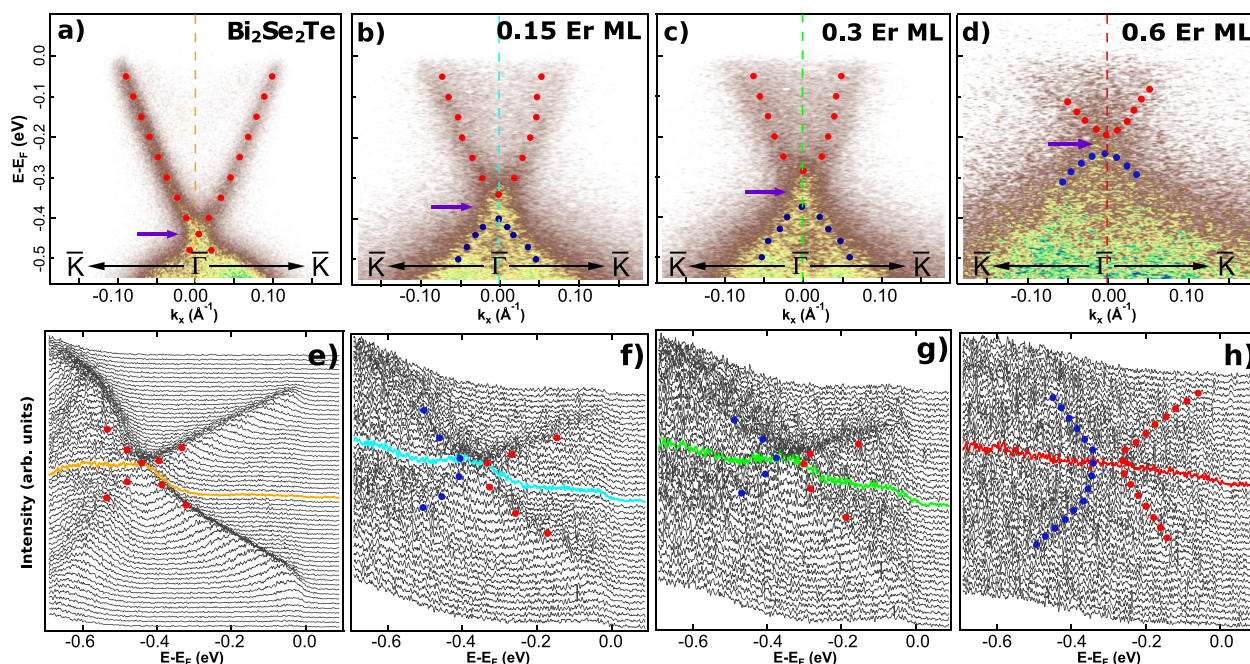


Figure 5. Topological surface state (TSS) band structure evolution upon Er doping showing signatures of the magnetically induced bandgap at the Dirac point (DP). (a)–(d) TSS bandmaps for pristine $\text{Bi}_2\text{Se}_2\text{Te}$ and 0.15, 0.3, and 0.6 Er monolayer-doped $\text{Bi}_2\text{Se}_2\text{Te}$, respectively, acquired with a photon energy of $h\nu = 52$ eV and at $T = 15$ K. (e)–(h) Energy distribution curves (EDC) extracted from the TSS bandmaps in (a)–(d). EDCs at the $\bar{\Gamma}$ point are highlighted following the color correspondence, and the fitting procedures followed for the momentum distribution curves (MDC) and EDC analysis are described in section VII in the SM. The TSS and top valence band dispersions obtained from the MDC fittings are indicated by red and blue dots on the TSS ARPES bandmaps in the top panels. Similarly, EDC fitting results are displayed in the bottom panel. The indicated band dispersion for 0.6 Er ML is, contrary to the other coverages, just a guide to the eye due to the impossibility of performing appropriate fits because of the low signal-to-noise ratio. Purple arrows indicate the DP energy, which is upshifted as the Er coverage is increased.

distribution curves (MDCs) close to the E_F , depicted above each TSS bandmap. The Fermi wavevectors k_F for 0.3 ML Er/ $\text{Bi}_2\text{Se}_2\text{Te}$ (blue MDC, Figure 3(h)) are asymmetric with respect to the $\bar{\Gamma}$ point, as compared to pristine $\text{Bi}_2\text{Se}_2\text{Te}$ (red MDC, Figure 3(g)), as a consequence of the different v_F of the two branches of the TSSs, of $(8.0 \pm 0.3) \times 10^5$ and $(1.2 \pm 0.1) \times 10^6$ m/s for the branches corresponding to the vertex and the flat face of the trigonal TSSs, respectively. A similar asymmetric band dispersion of the TSS was predicted for the $\text{MnBi}_2\text{Te}_4(0001)$ surface AFM state alongside the same TSS warping transition.⁴⁸

The evolution of the TSS as a function of the Er coverage is shown in Figure 5. TSS ARPES bandmaps along the $\bar{\Gamma}\bar{K}$ direction for pristine, 0.15, 0.3, and 0.6 ML Er/ $\text{Bi}_2\text{Se}_2\text{Te}$ are shown in Figure 5(a)–(d), respectively (second derivative bandmaps shown in Figures S9 and S10 in section VII in the SM). The corresponding energy distribution curves (EDCs) as a function of the Er coverage are presented in Figure 5(e)–(h), where the EDCs acquired precisely at the $\bar{\Gamma}$ point and thus crossing the DP (along vertical dashed lines in Figures 5(a)–(d)) are highlighted following the color correspondence. Here, orange, cyan, green, and red lines stand for pristine, 0.15, 0.3, and 0.6 ML Er/ $\text{Bi}_2\text{Se}_2\text{Te}$, respectively. The band dispersions have been obtained from the MDC and EDC fittings, whose results are indicated by red and blue dots in Figure 5 (a detailed analysis on the MDC and EDC fitting procedure is included in SM, section VII). The dispersion obtained from the pristine sample (Figures 5(a) and (e)) displays linear branches which clearly cross at the DP. Red and blue dots for the doped samples (Figure 5(b)–(h)) indicate the upper and bottom band dispersions relative to the DP.

As previously described, the transition from hexagonal to trigonal of the TSS symmetry when an out-of-plane magnetic moment is introduced is expected to be accompanied by a bandgap opening at the DP because of the TRS breaking.⁴⁷

A more detailed and comprehensive picture on the TSS band dispersion around the DP can be gathered from the EDC fits (Figure 5(e)–(h)), particularly in those obtained at the $\bar{\Gamma}$ point, extracted along vertical dashed lines in Figure 5(a)–(d) and highlighted in the same colors as in Figure 5(e)–(h). The fits for the colored EDCs in Figure 5(e)–(g) are shown in Figure S11 in section VII in the SM. For the pristine sample (Figure 5(e) and Figure S11(a)) the DP is clearly defined by the intersection of the two linear dispersive branches (orange EDC), resulting in a single, punctual, and sharp peak with a maximum intensity at 440 meV. After the Er deposition, a broadening of the intensity is clearly evidenced around the DP, as reflected in Figure 5 and more clearly in the second derivative bandmaps in Figures S9 and S10 in section VII in the SM, which would be an indication of a possible bandgap opening at the DP. Indeed, this energy broadening and the gap opening are unequivocally evidenced in the EDCs in Figures S11(c) and (e) where, instead of a single peak as for the pristine sample, two peaks are necessary for the correct fitting in the energy region close to the DP. Moreover, the dispersion of this double peak structure can be extracted from the EDC fittings in the vicinity of the $\bar{\Gamma}$ point (Figure S12) and is indicated by red and blue dots in Figure 5(f),(g). The characteristic linear dispersion of relativistic massless Dirac Fermions of the pristine sample seems to be renormalized to a parabolic-like dispersion, showing a plateau in the EDC intensity in the vicinity of the $\bar{\Gamma}$ point, while the cusp-like

shape of the top of the VB is preserved. This would be another indication of the bandgap between the top of the bulk VB and the bottom of the TSS. Similar XPS and ARPES results have been found after 0.3 Dy ML deposition and are summarized in section IV in the SM. All the details on the procedures followed for the fitting of the MDCs and EDCs, as well as for the determination of the TSS dispersions and the gap opening for the different samples, are included in Figures S9–S13 in section VII in the SM.

As discussed at the beginning of the manuscript, similar bandgap openings have already been experimentally observed and attributed to TRS by magnetic impurities for numerous transition metal magnetic impurities⁷ or Dy substitutional dopants.⁴¹ Nevertheless, the magnetically induced warping transition also resulting from the TRS breaking has not been reported so far.

In this work, by doping the surface of a TI with RE atoms, the magnetically induced evolution of the warping of the TSS from hexagonal to trigonal has been demonstrated by means of ARPES experiments. This shape transition has been predicted to be accompanied by a bandgap opening at the DP, and indeed, signatures of such an effect have also been observed in the present study. Additionally, the DP has been proven to be tunable toward the E_F through charge transfer between the RE adatoms and the substrate. The TSS band dispersion of the doped system is reproduced by including a Zeeman-like term in the low energy Hamiltonian describing the system. This modification entails two important consequences, the first of them being the just above-described breaking of the hexagonal symmetry and the second one the opening of a gap at the DP of the TSS. Both phenomena have been observed in the ARPES measurements. Moreover, we find that in order to theoretically describe the experimental results a large exchange coupling is needed, of the order of 0.1 eV. Thus, the large exchange coupling and the DP tunability make the controlled doping of TIs with REs an excellent approach to realize the QAHE at higher temperatures.

■ ASSOCIATED CONTENT

SI Supporting Information

The Supporting Information is available free of charge at <https://pubs.acs.org/doi/10.1021/acs.nanolett.3c00587>.

Additional experimental data and details on the sample growth methods and the theoretical model (PDF)

■ AUTHOR INFORMATION

Corresponding Author

Miguel A. Valbuena – *Instituto Madrileño de Estudios Avanzados, IMDEA Nanociencia, 28049 Madrid, Spain*;
orcid.org/0000-0002-0585-5636;
Email: miguelangel.valbuena@imdea.org

Authors

Beatriz Muñoz Cano – *Instituto Madrileño de Estudios Avanzados, IMDEA Nanociencia, 28049 Madrid, Spain*;
orcid.org/0000-0002-9338-7077
Yago Ferreira – *Instituto Madrileño de Estudios Avanzados, IMDEA Nanociencia, 28049 Madrid, Spain*
Pierre A. Pantaleón – *Instituto Madrileño de Estudios Avanzados, IMDEA Nanociencia, 28049 Madrid, Spain*
Ji Dai – *ALBA Synchrotron Light Source, 08290 Barcelona, Spain*

Massimo Tallarida – *ALBA Synchrotron Light Source, 08290 Barcelona, Spain*

Adriana I. Figueroa – *Departament de Física de la Matèria Condensada, Universitat de Barcelona, 08028 Barcelona, Spain; Catalan Institute of Nanoscience and Nanotechnology (ICN2), CSIC and BIST, Campus UAB, 08193 Barcelona, Spain*; orcid.org/0000-0002-8498-9383

Vera Marinova – *Institute of Optical Materials and Technologies, Bulgarian Academy of Sciences, Acad. G. Bontchev, 1113 Sofia, Bulgaria*; orcid.org/0000-0002-3499-0212

Kevin García-Díez – *ALBA Synchrotron Light Source, 08290 Barcelona, Spain; Catalan Institute of Nanoscience and Nanotechnology (ICN2), CSIC and BIST, Campus UAB, 08193 Barcelona, Spain*; orcid.org/0000-0001-8093-904X

Aitor Mugarza – *Catalan Institute of Nanoscience and Nanotechnology (ICN2), CSIC and BIST, Campus UAB, 08193 Barcelona, Spain; ICREA Institució Catalana de Recerca i Estudis Avançats, 08010 Barcelona, Spain*;
orcid.org/0000-0002-2698-885X

Sergio O. Valenzuela – *Catalan Institute of Nanoscience and Nanotechnology (ICN2), CSIC and BIST, Campus UAB, 08193 Barcelona, Spain; ICREA Institució Catalana de Recerca i Estudis Avançats, 08010 Barcelona, Spain*;
orcid.org/0000-0002-4632-8891

Rodolfo Miranda – *Instituto Madrileño de Estudios Avanzados, IMDEA Nanociencia, 28049 Madrid, Spain; Departamento de Física de la Materia Condensada, Instituto “Nicolás Cabrera” and Condensed Matter Physics Center (IFIMAC), Universidad Autónoma de Madrid (UAM), Campus de Cantoblanco, 28049 Madrid, Spain*

Julio Camarero – *Instituto Madrileño de Estudios Avanzados, IMDEA Nanociencia, 28049 Madrid, Spain; Departamento de Física de la Materia Condensada, Instituto “Nicolás Cabrera” and Condensed Matter Physics Center (IFIMAC), Universidad Autónoma de Madrid (UAM), Campus de Cantoblanco, 28049 Madrid, Spain*; orcid.org/0000-0003-0078-7280

Francisco Guinea – *Instituto Madrileño de Estudios Avanzados, IMDEA Nanociencia, 28049 Madrid, Spain; Donostia International Physics Center, 20018 San Sebastián, Spain; Ikerbasque, Basque Foundation for Science, 48009 Bilbao, Spain*

Jose Angel Silva-Guillén – *Instituto Madrileño de Estudios Avanzados, IMDEA Nanociencia, 28049 Madrid, Spain*;
orcid.org/0000-0002-0483-5334

Complete contact information is available at:

<https://pubs.acs.org/doi/10.1021/acs.nanolett.3c00587>

Notes

The authors declare no competing financial interest.

■ ACKNOWLEDGMENTS

IMDEA Nanociencia and IFIMAC acknowledge financial support from the Spanish Ministry of Science and Innovation through, respectively, “Severo Ochoa” (Grant CEX2020-001039-S) and “María de Maeztu” (Grant CEX2018-000805-M) Programmes for Centres of Excellence in R&D. This project has received funding from the Community of Madrid (CM) through project P2018/NMT-4321 (NANOMAG-COST), from Spanish Ministry of Economic Affairs and

Digital Transformation (MINECO) through projects SPGC2018-098613-B-C21 (SpOrQuMat), EQC2019-006304-P (Equipamiento científico), and PID2020-116181RB-C31 (SONANO BRAIN) and from Spanish Ministry of Science and Innovation (MICINN) and the Spanish Research Agency (AEI/10.13039/501100011033) through grants PID2021-123776NB-C21 (CONPHASETM), PID2019-107338RB-C65, and PID2019-111773RB-I00. ICN2 was funded by the CERCA Programme/Generalitat de Catalunya and supported by the Spanish Ministry of Economy and Competitiveness, MINECO, under Contract No. SEV-2017-0706. A.I.F., V.M., and S.O.V. acknowledge support from European Union's Horizon 2020 FET-PROACTIVE project TOCHA under Grant Agreement No. 824140. LOREA was cofunded by the European Regional Development Fund (ERDF) within the Framework of the Smart Growth Operative Programme 2014-2020. B.M.C. acknowledges support from CM (PEJD-2019-PRE/IND-17048). F.G. and P.A.P. acknowledge support from the European Commission, within the Graphene Flagship, Core 3 (Grant No. 881603), from CM (Grant NMAT2D) and (MAD2D-CM)-MRR MATERIALES AVANZADOS-IMDEA-NC. Y.F. acknowledges financial support through the Programa de Atracción de Talento de la Comunidad de Madrid, Spain, Grant No. 2018-T2/IND-11088. A.I.F. is a Serra Hùnter fellow. The authors acknowledge Jordi Prat and Pierluigi Gargiani for their invaluable technical support during experiments.

REFERENCES

- (1) Hasan, M. Z.; Kane, C. L. Colloquium: Topological insulators. *Rev. Mod. Phys.* **2010**, *82*, 3045.
- (2) Moore, J. E. The birth of topological insulators. *Nature* **2010**, *464*, 194–198.
- (3) Liu, J.; Hesjedal, T. Magnetic topological insulator heterostructures: A review. *Adv. Mater.* **2021**, *2102427*.
- (4) Yu, R.; Zhang, W.; Zhang, H.-J.; Zhang, S.-C.; Dai, X.; Fang, Z. Quantized anomalous Hall effect in magnetic topological insulators. *Science* **2010**, *329*, 61–64.
- (5) Fei, F.; Zhang, S.; Zhang, M.; Shah, S. A.; Song, F.; Wang, X.; Wang, B. The material efforts for quantized Hall devices based on topological insulators. *Adv. Mater.* **2019**, *32*, 1904593.
- (6) Xu, S.-Y.; Neupane, M.; Liu, C.; Zhang, D.; Richardella, A.; Andrew Wray, L.; Alidoust, N.; Leandersson, M.; Balasubramanian, T.; Sánchez-Barriga, J.; et al. Hedgehog spin texture and Berry's phase tuning in a magnetic topological insulator. *Nat. Phys.* **2012**, *8*, 616–622.
- (7) Chen, Y.; Chu, J.-H.; Analytis, J.; Liu, Z.; Igarashi, K.; Kuo, H.-H.; Qi, X.; Mo, S.-K.; Moore, R.; Lu, D.; et al. Massive Dirac fermion on the surface of a magnetically doped topological insulator. *Science* **2010**, *329*, 659–662.
- (8) Sessi, P.; Rüßmann, P.; Bathon, T.; Barla, A.; Kokh, K.; Tereshchenko, O.; Fauth, K.; Mahatha, S.; Valbuena, M.; Godey, S.; et al. Superparamagnetism-induced mesoscopic electron focusing in topological insulators. *Phys. Rev. B* **2016**, *94*, 075137.
- (9) Rüßmann, P.; Mahatha, S. K.; Sessi, P.; Valbuena, M. A.; Bathon, T.; Fauth, K.; Godey, S.; Mugarza, A.; Kokh, K. A.; Tereshchenko, O. E.; et al. Towards microscopic control of the magnetic exchange coupling at the surface of a topological insulator. *Journal of Physics: Materials* **2018**, *1*, 015002.
- (10) Otrokov, M. M.; Menshchikova, T. V.; Rusinov, I.; Vergniory, M.; Kuznetsov, V. M.; Chulkov, E. V. Magnetic extension as an efficient method for realizing the quantum anomalous hall state in topological insulators. *JETP Letters* **2017**, *105*, 297–302.
- (11) Kandala, A.; Richardella, A.; Rench, D.; Zhang, D.; Flanagan, T.; Samarth, N. Growth and characterization of hybrid insulating ferromagnet-topological insulator heterostructure devices. *Appl. Phys. Lett.* **2013**, *103*, 202409.
- (12) Hou, Y.; Kim, J.; Wu, R. Magnetizing topological surface states of Bi₂Se₃ with a CrI₃ monolayer. *Science advances* **2019**, *5*, eaaw1874.
- (13) Chang, C.-Z.; Zhang, J.; Feng, X.; Shen, J.; Zhang, Z.; Guo, M.; Li, K.; Ou, Y.; Wei, P.; Wang, L.-L.; et al. Experimental observation of the quantum anomalous Hall effect in a magnetic topological insulator. *Science* **2013**, *340*, 167–170.
- (14) Chang, C.-Z.; Zhao, W.; Kim, D. Y.; Zhang, H.; Assaf, B. A.; Heiman, D.; Zhang, S.-C.; Liu, C.; Chan, M. H.; Moodera, J. S. High-precision realization of robust quantum anomalous Hall state in a hard ferromagnetic topological insulator. *Nat. Mater.* **2015**, *14*, 473–477.
- (15) Otrokov, M. M.; Klimovskikh, I. I.; Bentmann, H.; Estyunin, D.; Zeugner, A.; Aliev, Z. S.; Gaß, S.; Wolter, A.; Koroleva, A.; Shikin, A. M.; et al. Prediction and observation of an antiferromagnetic topological insulator. *Nature* **2019**, *576*, 416–422.
- (16) Rienks, E. D.; Wimmer, S.; Sánchez-Barriga, J.; Caha, O.; Mandal, P. S.; Růžička, J.; Ney, A.; Steiner, H.; Volobuev, V. V.; Groiß, H.; et al. Large magnetic gap at the Dirac point in Bi₂Te₃/MnBi₂Te₄ heterostructures. *Nature* **2019**, *576*, 423–428.
- (17) Garnica, M.; Otrokov, M. M.; Aguilar, P. C.; Klimovskikh, I.; Estyunin, D.; Aliev, Z. S.; Amirasanov, I. R.; Abdullayev, N. A.; Zverev, V. N.; Babanly, M. B.; et al. Native point defects and their implications for the Dirac point gap at MnBi₂Te₄ (0001). *npj Quantum Materials* **2022**, *7*, 1–9.
- (18) Grauer, S.; Schreyeck, S.; Winnerlein, M.; Brunner, K.; Gould, C.; Molenkamp, L. Coincidence of superparamagnetism and perfect quantization in the quantum anomalous Hall state. *Phys. Rev. B* **2015**, *92*, 201304.
- (19) Pan, L.; Liu, X.; He, Q. L.; Stern, A.; Yin, G.; Che, X.; Shao, Q.; Zhang, P.; Deng, P.; Yang, C.-Y.; et al. Probing the low-temperature limit of the quantum anomalous Hall effect. *Science advances* **2020**, *6*, eaaz3595.
- (20) Gambardella, P.; Rusponi, S.; Veronese, M.; Dhesi, S.; Grazioli, C.; Dallmeyer, A.; Cabria, I.; Zeller, R.; Dederichs, P.; Kern, K.; et al. Giant magnetic anisotropy of single cobalt atoms and nanoparticles. *Science* **2003**, *300*, 1130–1133.
- (21) Wray, L. A.; Xu, S.-Y.; Xia, Y.; Hsieh, D.; Fedorov, A. V.; Hor, Y. S.; Cava, R. J.; Bansil, A.; Lin, H.; Hasan, M. Z. A topological insulator surface under strong Coulomb, magnetic and disorder perturbations. *Nat. Phys.* **2011**, *7*, 32–37.
- (22) Scholz, M.; Sánchez-Barriga, J.; Marchenko, D.; Varykhalov, A.; Volykhov, A.; Yashina, L.; Rader, O. Tolerance of topological surface states towards magnetic moments: Fe on Bi₂Se₃. *Phys. Rev. Lett.* **2012**, *108*, 256810.
- (23) Valla, T.; Pan, Z.-H.; Gardner, D.; Lee, Y.; Chu, S. Photoemission spectroscopy of magnetic and nonmagnetic impurities on the surface of the Bi₂Se₃ topological insulator. *Phys. Rev. Lett.* **2012**, *108*, 117601.
- (24) Honolka, J.; Khajetoorians, A.; Sessi, V.; Wehling, T.; Stepanow, S.; Mi, J.-L.; Iversen, B.; Schlenk, T.; Wiebe, J.; Brookes, N.; et al. In-plane magnetic anisotropy of Fe atoms on Bi₂Se₃(111). *Phys. Rev. Lett.* **2012**, *108*, 256811.
- (25) Beidenkopf, H.; Roushan, P.; Seo, J.; Gorman, L.; Drozdov, I.; Hor, Y. S.; Cava, R. J.; Yazdani, A. Spatial fluctuations of helical Dirac fermions on the surface of topological insulators. *Nat. Phys.* **2011**, *7*, 939–943.
- (26) Chang, C.-Z.; Zhang, J.; Liu, M.; Zhang, Z.; Feng, X.; Li, K.; Wang, L.-L.; Chen, X.; Dai, X.; Fang, Z.; et al. Thin films of magnetically doped topological insulator with carrier-independent long-range ferromagnetic order. *Advanced materials* **2013**, *25*, 1065–1070.
- (27) Zhang, J.; Chang, C.-Z.; Tang, P.; Zhang, Z.; Feng, X.; Li, K.; Wang, L.-L.; Chen, X.; Liu, C.; Duan, W.; et al. Topology-driven magnetic quantum phase transition in topological insulators. *Science* **2013**, *339*, 1582–1586.
- (28) Vobornik, I.; Panaccione, G.; Fujii, J.; Zhu, Z.-H.; Offi, F.; Salles, B. R.; Borgatti, F.; Torelli, P.; Rueff, J. P.; Ceolin, D.; et al.

Observation of distinct bulk and surface chemical environments in a topological insulator under magnetic doping. *J. Phys. Chem. C* **2014**, *118*, 12333–12339.

(29) Abdalla, L. B.; Seixas, L.; Schmidt, T.; Miwa, R.; Fazzio, A. Topological insulator $\text{Bi}_2\text{Se}_3(111)$ surface doped with transition metals: An ab initio investigation. *Phys. Rev. B* **2013**, *88*, 045312.

(30) Jensen, J.; Mackintosh, A. R. *Rare earth magnetism*; Clarendon Press Oxford, 1991.

(31) Harrison, S.; Collins-McIntyre, L.; Zhang, S.; Baker, A.; Figueroa, A.; Kellock, A.; Pushp, A.; Parkin, S.; Harris, J.; Van Der Laan, G.; et al. Study of Dy-doped Bi_2Te_3 : thin film growth and magnetic properties. *J. Phys.: Condens. Matter* **2015**, *27*, 245602.

(32) Singha, A.; Donati, F.; Wackerlin, C.; Baltic, R.; Dreiser, J.; Pivetta, M.; Rusponi, S.; Brune, H. Magnetic hysteresis in Er trimers on Cu (111). *Nano Lett.* **2016**, *16*, 3475–3481.

(33) Singha, A.; Baltic, R.; Donati, F.; Wackerlin, C.; Dreiser, J.; Persichetti, L.; Stepanow, S.; Gambardella, P.; Rusponi, S.; Brune, H. 4f occupancy and magnetism of rare-earth atoms adsorbed on metal substrates. *Phys. Rev. B* **2017**, *96*, 224418.

(34) Bellini, V.; Rusponi, S.; Koloenc, J.; Mahatha, S. K.; Valbuena, M. A.; Persichetti, L.; Pivetta, M.; Sorokin, B. V.; Merk, D.; Reynaud, S.; et al. Slow Magnetic Relaxation of Dy Adatoms with In-Plane Magnetic Anisotropy on a Two-Dimensional Electron Gas. *ACS Nano* **2022**, *16*, 11182–11193.

(35) Baltic, R.; Pivetta, M.; Donati, F.; Wackerlin, C.; Singha, A.; Dreiser, J.; Rusponi, S.; Brune, H. Superlattice of single atom magnets on graphene. *Nano Lett.* **2016**, *16*, 7610–7615.

(36) Ormazá, M.; Fernández, L.; Ilyn, M.; Magana, A.; Xu, B.; Verstraete, M.; Gastaldo, M.; Valbuena, M.; Gargiani, P.; Mugarza, A.; et al. High temperature ferromagnetism in a GdAg_2 monolayer. *Nano Lett.* **2016**, *16*, 4230–4235.

(37) Fernández, L.; Blanco-Rey, M.; Castrillo-Bodero, R.; Ilyn, M.; Ali, K.; Turco, E.; Corso, M.; Ormazá, M.; Gargiani, P.; Valbuena, M. A.; et al. Influence of 4f filling on electronic and magnetic properties of rare earth-Au surface compounds. *Nanoscale* **2020**, *12*, 22258–22267.

(38) Fornari, C. I.; Bentmann, H.; Morelhão, S. L.; Peixoto, T. R.; Rapp, P. H.; Tcakaev, A.-V.; Zabolotnyy, V.; Kamp, M.; Lee, T.-L.; Min, C.-H.; et al. Incorporation of europium in Bi_2Te_3 topological insulator epitaxial films. *J. Phys. Chem. C* **2020**, *124*, 16048–16057.

(39) Tcakaev, A.; Zabolotnyy, V. B.; Fornari, C. I.; Rüßmann, P.; Peixoto, T. R.; Stier, F.; Dettbarn, M.; Kagerer, P.; Weschke, E.; Schierle, E.; et al. Incipient antiferromagnetism in the Eu-doped topological insulator Bi_2Te_3 . *Phys. Rev. B* **2020**, *102*, 184401.

(40) Kim, J.; Lee, K.; Takabatake, T.; Kim, H.; Kim, M.; Jung, M.-H. Magnetic transition to antiferromagnetic phase in gadolinium substituted topological insulator Bi_2Te_3 . *Sci. Rep.* **2015**, *5*, 10309.

(41) Harrison, S.; Collins-McIntyre, L. J.; Schönherr, P.; Vailionis, A.; Srot, V.; van Aken, P. A.; Kellock, A.; Pushp, A.; Parkin, S.; Harris, J.; et al. Massive Dirac fermion observed in lanthanide-doped topological insulator thin films. *Sci. Rep.* **2015**, *5*, 15767.

(42) Hesjedal, T. Rare earth doping of topological insulators: A brief review of thin film and heterostructure systems. *Physica Status Solidi A* **2019**, *216*, 1800726.

(43) Duffy, L. B.; Steinke, N.-J.; Krieger, J.; Figueroa, A. I.; Kummer, K.; Lancaster, T.; Giblin, S. R.; Pratt, F. L.; Blundell, S. J.; Prokscha, T.; et al. Microscopic effects of Dy doping in the topological insulator Bi_2Te_3 . *Phys. Rev. B* **2018**, *97*, 174427.

(44) Figueroa, A. I.; Bonell, F.; Cuxart, M.; Valvidares, M.; Gargiani, P.; van der Laan, G.; Mugarza, A.; Valenzuela, S. O. Absence of Magnetic Proximity Effect at the Interface of Bi_2Se_3 and $(\text{Bi}, \text{Sb})_2\text{Te}_3$ with EuS. *Phys. Rev. Lett.* **2020**, *125*, 226801.

(45) He, K. MnBi_2Te_4 -family intrinsic magnetic topological materials. *npj Quantum Materials* **2020**, *5*, 90.

(46) Imai, Y.; Yamaguchi, T.; Yamakage, A.; Kohno, H. Spintronic properties of topological surface Dirac electrons with hexagonal warping. *Phys. Rev. B* **2021**, *103*, 054402.

(47) Naselli, G.; Moghaddam, A. G.; Di Napoli, S.; Vildosola, V.; Fulga, I. C.; van den Brink, J.; Facio, J. I. Magnetic warping in topological insulators. *Physical Review Research* **2022**, *4*, 033198.

(48) Tan, H.; Kaplan, D.; Yan, B. Momentum-inversion symmetry breaking on the Fermi surface of magnetic topological insulators. *Phys. Rev. Mater.* **2022**, *6*, 104204.

(49) Wang, D.; Wang, H.; Xing, D.; Zhang, H. Three-Dirac-fermion approach to unexpected gapless surface states of van der Waals magnetic topological insulators. *Arxiv* **2022**, DOI: 10.48550/arXiv.2205.08204.

(50) Wang, L.-L.; Johnson, D. D. Ternary tetradymite compounds as topological insulators. *Phys. Rev. B* **2011**, *83*, 241309.

(51) García, G.; Martín, M.; Ynsa, M.; Torres-Costa, V.; Crespillo, M.; Tardío, M.; Olivares, J.; Bosia, F.; Peña-Rodríguez, O.; Nicolas, J.; et al. Process design for the manufacturing of soft X-ray gratings in single-crystal diamond by high-energy heavy-ion irradiation. *Eur. Phys. J. Plus* **2022**, *137*, 1157.

(52) Crisol, A.; Bisti, F.; Colldelram, C.; Llonch, M.; Molas, B.; Monge, R.; Nicolás, J.; Nikitina, L.; Quispe, M.; Ribó, L.; Tallarida, M. ALBA BL20 New Monochromator Design. *Proc. MEDSI'20* **2021**, 14–16.

(53) Banister, J.; Legvold, S.; Spedding, F. Structure of Gd, Dy, and Er at low temperatures. *Phys. Rev.* **1954**, *94*, 1140.

(54) Maaß, H.; Schreyeck, S.; Schatz, S.; Fiedler, S.; Seibel, C.; Lutz, P.; Karczewski, G.; Bentmann, H.; Gould, C.; Brunner, K.; et al. Electronic structure and morphology of epitaxial Bi_2Te_3 topological insulator films. *J. Appl. Phys.* **2014**, *116*, 193708.

(55) Walsh, L. A.; Smyth, C. M.; Barton, A. T.; Wang, Q.; Che, Z.; Yue, R.; Kim, J.; Kim, M. J.; Wallace, R. M.; Hinkle, C. L. Interface chemistry of contact metals and ferromagnets on the topological insulator Bi_2Se_3 . *J. Phys. Chem. C* **2017**, *121*, 23551–23563.

(56) Cuxart, M. G.; Valbuena, M. A.; Robles, R.; Moreno, C.; Bonell, F.; Sauthier, G.; Imaz, I.; Xu, H.; Nistor, C.; Barla, A.; et al. Molecular approach for engineering interfacial interactions in magnetic/topological insulator heterostructures. *ACS Nano* **2020**, *14*, 6285–6294.

(57) Miyamoto, K.; Kimura, A.; Okuda, T.; Miyahara, H.; Kuroda, K.; Namatame, H.; Taniguchi, M.; Ereemeev, S.; Menshchikova, T. V.; Chulkov, E. V.; et al. Topological surface states with persistent high spin polarization across the Dirac point in Bi_2Te_3 and Bi_2Se_3 . *Phys. Rev. Lett.* **2012**, *109*, 166802.

(58) Bao, L.; He, L.; Meyer, N.; Kou, X.; Zhang, P.; Chen, Z.-g.; Fedorov, A. V.; Zou, J.; Riedemann, T. M.; Lograsso, T. A.; et al. Weak anti-localization and quantum oscillations of surface states in topological insulator Bi_2Se_3 . *Sci. Rep.* **2012**, *2*, 726.

(59) Netsou, A.-M.; Muzychenko, D. A.; Dausy, H.; Chen, T.; Song, F.; Schouteden, K.; Van Bael, M. J.; Van Haesendonck, C. Identifying native point defects in the topological insulator Bi_2Te_3 . *ACS Nano* **2020**, *14*, 13172–13179.

(60) Figueroa, A.; Van Der Laan, G.; Harrison, S.; Cibin, G.; Hesjedal, T. Oxidation effects in rare earth doped topological insulator thin films. *Sci. Rep.* **2016**, *6*, 22935.

(61) Fu, L. Hexagonal warping effects in the surface states of the topological insulator Bi_2Te_3 . *Phys. Rev. Lett.* **2009**, *103*, 266801.

(62) Chen, Y.; Analytis, J. G.; Chu, J.-H.; Liu, Z.; Mo, S.-K.; Qi, X.-L.; Zhang, H.; Lu, D.; Dai, X.; Fang, Z.; et al. Experimental realization of a three-dimensional topological insulator, Bi_2Te_3 . *Science* **2009**, *325*, 178–181.

(63) Arakane, T.; Sato, T.; Souma, S.; Kosaka, K.; Nakayama, K.; Komatsu, M.; Takahashi, T.; Ren, Z.; Segawa, K.; Ando, Y. Tunable Dirac cone in the topological insulator $\text{Bi}_{1-x}\text{Sb}_x\text{Te}_3$. *Nat. Commun.* **2012**, *3*, 636.

(64) Xia, Y.; Qian, D.; Hsieh, D.; Wray, L.; Pal, A.; Lin, H.; Bansil, A.; Grauer, D.; Hor, Y. S.; Cava, R. J.; et al. Observation of a large-gap topological-insulator class with a single Dirac cone on the surface. *Nat. Phys.* **2009**, *5*, 398–402.

(65) Qi, X.-L.; Wu, Y.-S.; Zhang, S.-C. Topological quantization of the spin Hall effect in two-dimensional paramagnetic semiconductors. *Phys. Rev. B* **2006**, *74*, 085308.

(66) Nomura, K.; Nagaosa, N. Electric charging of magnetic textures on the surface of a topological insulator. *Phys. Rev. B* **2010**, *82*, 161401.

(67) Yokoyama, T.; Zang, J.; Nagaosa, N. Theoretical study of the dynamics of magnetization on the topological surface. *Phys. Rev. B* **2010**, *81*, 241410.

(68) Yokoyama, T. Current-induced magnetization reversal on the surface of a topological insulator. *Phys. Rev. B* **2011**, *84*, 113407.

(69) Ferreira, Y.; Buijnsters, F.; Katsnelson, M. Dirac electrons and domain walls: A realization in junctions of ferromagnets and topological insulators. *Phys. Rev. B* **2015**, *92*, 085416.

(70) Liu, Q.; Liu, C.-X.; Xu, C.; Qi, X.-L.; Zhang, S.-C. Magnetic impurities on the surface of a topological insulator. *Phys. Rev. Lett.* **2009**, *102*, 156603.

(71) Ferreira, Y.; Cortijo, A. Domain wall motion in junctions of thin-film magnets and topological insulators. *Phys. Rev. B* **2014**, *89*, 024413.

Recommended by ACS

Giant and Tunable Out-of-Plane Spin Polarization of Topological Antimonene

Polina M. Sheverdyaeva, Paolo Moras, *et al.*

JULY 17, 2023
NANO LETTERS

READ 

Controlling the Interlayer Dzyaloshinskii–Moriya Interaction by Electrical Currents

Fabian Kammerbauer, Mathias Kläui, *et al.*

JULY 19, 2023
NANO LETTERS

READ 

Tunable Topological States in Stacked Chern Insulator Bilayers

Xuanyi Li, Sheng Meng, *et al.*

MARCH 28, 2023
NANO LETTERS

READ 

Topological Hall Signatures of Two Chiral Spin Textures Hosted in a Single Tetragonal Inverse Heusler Thin Film

Pranava K. Sivakumar, Stuart S. P. Parkin, *et al.*

SEPTEMBER 28, 2020
ACS NANO

READ 

Get More Suggestions >